

Hide-and-Seek Attribution: Weakly Supervised Segmentation of Vertebral Metastases in CT

Matan Atad^{1,2*}, Alexander W. Marka³, Lisa Steinhelfer², Anna Curto-Vilalta^{2,8},
Yannik Leonhardt³, Sarah C. Foreman¹, Anna-Sophia Walburga Dietrich^{1,7}, Robert Graf^{1,2},
Alexandra S. Gersing⁴, Bjoern Menze⁵, Daniel Rueckert^{2,6}, Jan S. Kirschke^{1,2}, Hendrik Möller^{1,2}

¹Institute of Neuroradiology, TUM University Hospital, Technical University of Munich (TUM), Germany

²Chair for AI in Healthcare and Medicine, TUM and TUM University Hospital, Munich, Germany

³Institute of Diagnostic and Interventional Radiology, TUM University Hospital, Germany

⁴Department of Neuroradiology, University Hospital Munich (LMU), Germany

⁵Department of Quantitative Biomedicine, University of Zurich, Switzerland

⁶Department of Computing, Imperial College London, UK

⁷Department of Diagnostic and Interventional Radiology, University Hospital Frankfurt, Germany

⁸Department of Orthopedics and Sports Orthopedics, TUM University Hospital, Germany

December 9, 2025

Abstract

Accurate segmentation of vertebral metastasis in CT is clinically important yet difficult to scale, as voxel-level annotations are scarce and both lytic and blastic lesions often resemble benign degenerative changes. We introduce a weakly supervised method trained solely on vertebra-level healthy/malignant labels, without any lesion masks. The method combines a Diffusion Autoencoder (DAE) that produces a classifier-guided healthy edit of each vertebra with pixel-wise difference maps that propose candidate lesion regions. To determine which regions truly reflect malignancy, we introduce Hide-and-Seek Attribution: each candidate is revealed in turn while all others are hidden, the edited image is projected back to the data manifold by the DAE, and a latent-space classifier quantifies the isolated malignant contribution of that component. High-scoring regions form the final lytic or blastic segmentation. On held-out radiologist annotations, we achieve strong blastic/lytic performance despite no mask supervision (F1: 0.91/0.85; Dice: 0.87/0.78), exceeding baselines (F1: 0.79/0.67; Dice: 0.74/0.55). These results show that vertebra-level labels can be transformed into reliable lesion masks, demonstrating that generative editing combined with selective occlusion supports accurate weakly supervised segmentation in CT.

1 Introduction

Bone metastases are among the most frequent complications of advanced cancer, with the skeleton being the third most common metastatic site, typically arising from breast, prostate, and lung primary sites [5]. Spinal involvement is particularly consequential: vertebral lesions can cause severe pain, mechanical instability, fractures, and spinal cord compression [5]. Reliable monitoring is therefore essential to detect progression early and guide interventions to prevent structural failure and neurological compromise.

*Corresponding author: matan.atad@tum.de

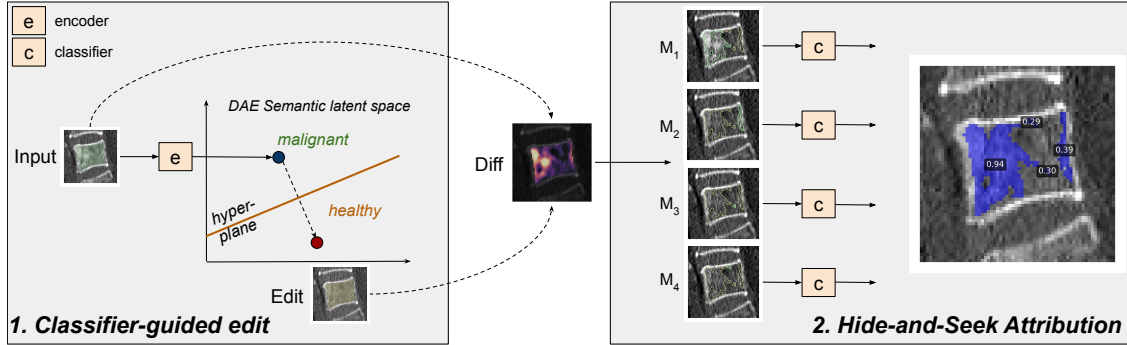


Figure 1: Weakly supervised vertebral lesion segmentation from image-level labels. (1) Classifier-guided healthy edit (yellow) is generated in DAE latent space from the original (green). Difference maps produce suspect lesions. (2) Hide-and-Seek isolates each candidate (green contours), occludes the others (yellow), and computes normalized Δ -scores. Thresholding these scores yields the final masks.

Vertebral metastases are routinely evaluated on CT in standard oncologic staging, together with MRI and nuclear medicine imaging [32]. Interpretation is difficult because malignant lesions vary in appearance and may resemble benign age-related findings such as trabecular rarefaction, Modic endplate changes, or Schmorl nodes [26]. Assessment is mostly qualitative because many lesions have diffused margins and no clear measurable boundaries [37]. Metastases manifest as lytic (bone loss), blastic (bone formation), or mixed, with primary tumors showing characteristic but non-exclusive patterns (e.g., myeloma often lytic, prostate cancer often blastic, breast cancer frequently mixed) [22]. On CT, lytic components appear hypodense and blastic components hyperdense [5]. Automated segmentation can provide reproducible delineation of metastatic lesions, which is particularly important when several lesions occur in the same vertebra. Accurate masks enable downstream analyses, such as estimating vertebral stability or measuring progression, that are difficult to perform from qualitative CT assessment.

Existing methods for automated vertebral lesion segmentation are fully supervised and require costly voxel-level annotations [6, 10, 11, 24]. Weakly supervised strategies could reduce this annotation burden, but have inherent limitations: CAM-based methods [7, 18, 25, 31] highlight the most discriminative pixels and may miss multiple lesions. Medical SAM [9, 21] require precise bounding box prompts and cannot determine pathology without finetuning. Pseudo-healthy reconstruction approaches [16, 38] detect deviations from normal anatomy but are not able to reliably separate malignancy from benign findings. Finally, classifier-guided healthy reconstructions [17, 34] provide more complete residuals but may introduce artifacts influenced by data bias [3]. These limitations motivate an approach that evaluates suspected lesions directly.

Occlusion-based attribution methods hide or replace image regions to quantify their influence on a classifier’s output [1, 15, 35]. Building on this idea, we selectively occlude candidate regions obtained from classifier-guided healthy edits, reconstruct each edit with a generative model, and measure how strongly that region alone increases the malignancy score. Although healthy edits introduce spurious artifacts, our hypothesis is that such artifacts, being unrelated to malignancy, will not yield high scores and will therefore be suppressed. This enables weakly supervised, lesion-level segmentation without requiring dense ground-truth masks.

Our contributions are as follows: (1) We introduce weakly supervised lesion segmentation for vertebral metastases, a clinically important and technically challenging task with no prior works, achieving Dice scores of 0.87 (blastic) and 0.78 (lytic). (2) We propose *Hide-and-Seek*

Attribution, a novel occlusion-based strategy that evaluates suspected lesions by selectively hiding alternatives, reconstructing the image via a Diffusion Autoencoder (DAE), and quantifying each region’s independent malignant contribution. (3) We benchmark our method against multiple weakly supervised baselines and analyze its limitations. Our code is available at https://github.com/matanat/hide_and_seek.

2 Related Work

Weakly supervised segmentation in medical imaging. Segmentation based on image-level labels has been widely explored as an alternative to tedious voxel-level annotation in medical imaging. Most methods rely on classifier-derived Class Activation Maps (CAMs) [7, 18, 25, 31] to generate coarse pseudo-masks, which are then refined and used to train fully supervised segmentation models [8, 36, 39]. Nevertheless, CAMs remain intrinsically sparse, tending to highlight only the most discriminative pixels rather than all occurrences of a visual concept of interest.

Adaptations of Segment Anything (SAM) [19] have also been applied for medical tasks [9, 21]. These models perform well when provided with tight bounding-box prompts, but cannot determine whether a region is pathological without finetuning, restricting their utility.

Generative anomaly detection approaches reconstruct pseudo-healthy images and detect abnormalities via residuals [16, 17, 38]. While effective for highlighting deviations from normal anatomy, they cannot distinguish the target pathology from benign co-occurring changes. [34] employ a conditional GAN to generate healthy reconstructions and derive kidney-tumor masks from residuals, though GAN inpainting is prone to reproducing dataset biases [3]. Recently, [23] applied such edits to increase robustness in fully supervised organ segmentation. Their setting differs fundamentally from ours, as our goal is to segment the metastatic tissue itself.

Multiple-instance learning (MIL) offers another paradigm by optimizing bag-level classification to highlight multiple regions [2, 28]. However, MIL infers instance relevance only in the context of the full bag, so scores do not reflect a candidate’s standalone contribution. Our method evaluates each candidate in isolation using healthy edits, enabling per-candidate attribution that MIL does not provide.

Spinal lesion segmentation in CT. Existing work on spinal metastasis segmentation is exclusively based on full supervision. Multiple studies report only moderate Dice scores [6, 10, 11, 24].¹ These results suggest that vertebral lesions remain difficult to segment reliably even under strong supervision. Longitudinal-based approaches [27, 30] detect interval changes but require multi-timepoint imaging and cannot distinguish malignancy from other developed disease. Methods occasionally described as “weakly-supervised” [33] still rely on manually corrected masks and therefore do not correspond to the setting considered here. To our knowledge, weakly supervised segmentation of spinal metastasis has not been previously explored.

3 Dataset

CT scans from 440 patients were collected at the TUM University Hospital (mean age 67.5 ± 12.9 years; 211 female, 229 male). Each scan was reviewed by a radiologist with expertise in spinal imaging (A.S.W.D., 10 years of experience) who assigned vertebra-level labels (healthy vs.

¹[6] reported a Dice of 0.83 for lytic lesions. [11] reported Dice of 0.71 for lytic and 0.61 for blastic lesions with fully supervised training.

malignant)². Vertebrae with fractures were excluded, as lesion delineation in fractured vertebrae is highly challenging on CT [13]. Because cervical levels appeared only in a minority of scans, this study focuses on the thoracic and lumbar spine. The dataset was divided into three parts (Table 3): (1) The generative model was trained on 2d slices of all 5,644 vertebrae remaining after exclusions, without using any labels. (2) A classifier-training subset of 565 vertebrae (300 healthy, 265 malignant) was used to learn the latent healthy–malignant direction. (3) Quantitative evaluation was performed on a held-out test set of 17 patients (94 malignant vertebrae: 50 blastic, 16 lytic, and 28 mixed vertebrae). Two radiologists (L.S. and A.W.M. with 6 and 4 years of experience, respectively; A.W.M. supervised by Y.L., a board-certified radiologist) independently annotated all vertebrae: the first set (A) served as ground truth for all evaluations, and the second (B) was used for inter-rater agreement.

Table 1: Data usage in this study

Feature	Full dataset	Classifier subset	Test set (held-out)
Vertebrae	5,644	565	94
Healthy / malignant	4,972 / 672	300 / 265	0 / 94
Blastic / lytic / mixed	unknown	unknown	50 / 16 / 28
Used annotations	none	Image-level (healthy/malignant)	Pixel-level (lytic/blastic)
Purpose	Train DAE	Train classifier	Evaluation

4 Methods

We propose a weakly supervised method that segments vertebral lesions by testing the malignant contribution of each suspect region with a classifier (Figure 1). As input, we use the central sagittal slice extracted from each CT volume. We first reconstruct a healthy approximation of this slice with a DAE and derive lesions as residual differences. Each candidate region is then evaluated independently using Hide-and-Seek Attribution: all other candidates are masked in the original image, the edited image is reconstructed and re-encoded, and the resulting latent is scored by the classifier. The derived malignancy score reflects how strongly the candidate elevates the malignant signal, enabling retention of only true lytic or blastic regions without pixel-level supervision.

Unsupervised pretraining. A Diffusion Autoencoder (DAE) [29] is used to obtain a semantic latent representation of input CT slices. The model consists of a semantic encoder that maps an input image to a latent vector \vec{z}_{sem} and a diffusion-based decoder that reconstructs the image from this latent; both are trained jointly end-to-end. The resulting latent space has been shown to capture anatomical structure in an approximately linear and interpretable form [29]. Training is fully unsupervised and uses 2d mid-sagittal vertebral CT slices without lesion labels or masks.

Healthy edit. A logistic regression fitted to \vec{z}_{sem} provides a semantic direction separating healthy from malignant vertebrae. Its output $c(\cdot) \rightarrow [0, 1]$ represents the malignancy probability. Because the classifier is linear, its decision boundary is the hyperplane $\vec{n} \cdot \vec{z} + b = 0$, where \vec{n} is the learned normal vector and b is a bias term. The signed distance of a latent \vec{z} to this hyperplane is given by $\text{dist}(\vec{z}) = (\vec{n} \cdot \vec{z} + b) / \|\vec{n}\|$. To obtain a *healthy reconstruction*, we compute a closed-form edit of the latent that moves it to a predefined logit value. We convert a small target probability $p_{\text{target}} \approx 0$

²Labeling protocol described in [13].

into its corresponding logit d_{target} , and then project the original latent onto that point along the classifier’s normal direction:

$$\vec{z}_{\text{healthy}} = \vec{z} - (\text{dist}(\vec{z}) - d_{\text{target}}) \frac{\vec{n}}{\|\vec{n}\|}. \quad (1)$$

This transformation suppresses the malignant component encoded in the latent representation while preserving the vertebra’s anatomical identity.

Hide-and-Seek Attribution. Given a malignant vertebral slice I with latent \vec{z} , Hide-and-Seek Attribution begins by generating a healthy reconstruction I_{healthy} from the edited latent \vec{z}_{healthy} ³. Candidate abnormalities are identified from the residual map $D = I - I_{\text{healthy}}$ which is decomposed into $D^+ = \max(D, 0)$ and $D^- = \max(-D, 0)$, capturing lytic-like (brightening) and blastic-like (darkening) deviations from the healthy appearance. Each difference map is binarized, and connected-component analysis is applied to extract initial lesion candidates.

For each suspected component M , we isolate its effect by hiding all other candidates. Let Ω_M be the pixel set of M and Ω_{others} the union of all remaining suspected regions. Then:

$$I_{\text{hide}}(M)(x) = \begin{cases} I(x), & x \in \Omega_M, \\ I_{\text{healthy}}(x), & x \in \Omega_{\text{others}}, \\ I(x), & \text{otherwise,} \end{cases} \quad (2)$$

i.e., the appearance of M is preserved while all other suspected regions are replaced by their healthy reconstruction. We further reconstruct and encode $I_{\text{hide}}(M)$ into $\vec{z}_{\text{hide}}(M)$, projecting the edited image back onto the data manifold, to obtain an anatomically plausible version of the occluded slice.

Finally, the malignancy score of component M is defined as:

$$\Delta(M) = \frac{c(\vec{z}_{\text{hide}}(M)) - c(\vec{z}_{\text{healthy}})}{c(\vec{z}) - c(\vec{z}_{\text{healthy}}) + \varepsilon}, \quad (3)$$

where ε ensures numerical stability. The score $\Delta(M) \geq 0$ quantifies the fraction of the original malignancy probability linked to component M : values near 1 indicate that M explains most of the malignant evidence, whereas values near 0 reflect negligible influence. Components satisfying $\Delta(M) \geq \tau$ for some $\tau > 0$ are retained, with D^+ yielding the lytic mask and D^- the blastic mask. Because D^+ and D^- are disjoint by construction, the resulting masks do not overlap.

Implementation details All CT scans were resampled to 0.8 mm isotropic resolution. Vertebral structures were segmented using SpineR (Bonescreen GmbH⁴), providing both vertebral masks and anatomical level labels. For each vertebra, a $64 \times 64 \times 64$ crop centered on the vertebral body was extracted, and one sagittal slice from the central five was used as input to the DAE. The DAE was trained for 2206 epochs (93h 41m) on a single NVIDIA A40 GPU using the implementation of [29]. Healthy edits were obtained using a logistic regression classifier trained on semantic latents (F1: 0.90, AUC: 0.97). During inference, the segmentation pipeline is applied only to vertebrae predicted as malignant by the classifier, mirroring clinical workflow.

Difference maps are binarized using a per-image mean threshold, and Δ is thresholded at a fixed value of $\tau = 0.5$. Additional preprocessing and training details are provided in appendix A.1.2.

³Algorithm pseudocode is provided in appendix A.1.1.

⁴<https://www.bonescreen.de>

For fair comparison across methods, predictions are restricted to the vertebral body: the corpus mask from preprocessing is eroded to avoid boundary spillover, and only pixels within this region are retained. Finally, predicted components smaller than 5 pixels are removed uniformly across methods to suppress isolated noise.

Evaluation metrics Predictions are evaluated using Panoptica [20]. Predicted and reference lesions are matched using positive-Dice assignment with a many-to-one scheme to avoid penalizing over-segmentation. **Detection F1** (RQ) quantifies lesion detection: a lesion is considered detected if any prediction overlaps it (Dice > 0), and the F1-score summarizes precision and recall across all lesions. **Instance Dice** (SQ) is computed only for matched lesion pairs and reports the mean Dice overlap of correctly detected lesions. **Panoptic Dice** (PQ_D) integrates detection and segmentation as $PQ_D = RQ \times SQ$. **ASSD** is computed per matched pair to assess boundary accuracy and averaged across lesions. **Global Dice** is a voxel-wise Dice over the entire vertebral body, obtained by merging all predicted components and comparing them to the merged ground-truth mask. Metrics are reported separately for blastic, lytic, and mixed lesions, with mixed vertebrae evaluated as their own category since most baselines cannot distinguish lesion subtypes.

5 Results

We evaluate performance across baseline families, inter-rater agreement, and lesion-wise behavior of the proposed method.

Baseline methods. The proposed method was compared to representative weakly supervised segmentation methods spanning intensity-based, attribution-based, foundation-model, and anomaly detection. Specifically, we include naive Otsu thresholding, GradCAM / GradCAM++ / LayerCAM / EigenCAM [7, 18, 25, 31], MedSAM [21], and pseudo-healthy anomaly detection (AD). Baseline implementation details are provided in appendix A.1.3.

Inter-rater agreement. To characterize the inherent difficulty of the task, annotations from a second radiologist (B) were compared against the primary rater (A) (Tables A.3.1 and A.3.1 in the appendix). Agreement was high for blastic lesions (Detection F1 0.84, Instance Dice 0.81) but substantially lower for lytic lesions (Detection F1 0.51, Instance Dice 0.51), with B missing 25% of A’s lesions and marking 45% additional findings. ASSD remained low for both phenotypes (1.19 and 1.00, respectively), indicating that when both raters identified the same lesion, their boundary placement was largely consistent.

Overall segmentation performance. Segmentation accuracy across lesion phenotypes is summarized in Table 5. For blastic lesions, the proposed method reaches a Detection F1 of 0.91 ± 0.17 (vs. 0.79 ± 0.23 for the best CAM baseline and 0.72 ± 0.23 for AD), with Instance Dice increasing from 0.74 ± 0.11 (Otsu) to 0.87 ± 0.16 and Global Dice from 0.74 ± 0.08 to 0.88 ± 0.14 , alongside the lowest ASSD. For lytic lesions, Detection F1 rises from 0.67 ± 0.23 (MedSAM) to 0.85 ± 0.21 , and Instance Dice from 0.55 ± 0.23 (Otsu) to 0.78 ± 0.24 , with the lowest ASSD and highest Global Dice among all methods. Mixed lesions remain challenging for all approaches, but the proposed method attains the highest Instance Dice (0.62 ± 0.18), the highest Global Dice (0.62 ± 0.20), and the lowest ASSD (1.02 ± 0.53).

Table 2: Instance-level and global segmentation metrics (mean \pm SD) for Otsu, CAM-based baselines, MedSAM, anomaly detection (AD), and our method. Arrows indicate preferred direction; bold values denote the best score per metric.

Metric	Otsu	GradCAM	GradCAM++	LayerCAM	EigenCAM	MedSAM	AD	Ours
<i>Blastic lesions</i>								
Detection F1 (RQ) \uparrow	0.68 \pm 0.24	0.79 \pm 0.23	0.77 \pm 0.28	0.75 \pm 0.24	0.68 \pm 0.34	0.64 \pm 0.28	0.72 \pm 0.28	0.91 \pm 0.17
Instance Dice (SQ) \uparrow	0.74 \pm 0.11	0.43 \pm 0.19	0.43 \pm 0.20	0.39 \pm 0.18	0.38 \pm 0.22	0.44 \pm 0.22	0.53 \pm 0.22	0.87 \pm 0.16
Panoptic Dice (PQ _D) \uparrow	0.49 \pm 0.18	0.34 \pm 0.19	0.35 \pm 0.20	0.28 \pm 0.13	0.31 \pm 0.21	0.31 \pm 0.21	0.38 \pm 0.20	0.80 \pm 0.24
ASSD \downarrow	1.36 \pm 0.63	4.50 \pm 2.12	4.71 \pm 2.02	4.35 \pm 1.78	4.68 \pm 1.94	4.07 \pm 1.98	2.75 \pm 1.75	0.89 \pm 1.17
Global Dice \uparrow	0.74 \pm 0.08	0.42 \pm 0.18	0.41 \pm 0.20	0.36 \pm 0.15	0.37 \pm 0.20	0.45 \pm 0.22	0.54 \pm 0.22	0.88 \pm 0.14
<i>Lytic lesions</i>								
Detection F1 (RQ) \uparrow	0.64 \pm 0.23	0.56 \pm 0.33	0.53 \pm 0.31	0.54 \pm 0.25	0.43 \pm 0.32	0.67 \pm 0.23	0.32 \pm 0.38	0.85 \pm 0.21
Instance Dice (SQ) \uparrow	0.55 \pm 0.23	0.25 \pm 0.17	0.30 \pm 0.21	0.32 \pm 0.16	0.27 \pm 0.22	0.54 \pm 0.19	0.24 \pm 0.28	0.78 \pm 0.25
Panoptic Dice (PQ _D) \uparrow	0.35 \pm 0.18	0.14 \pm 0.10	0.17 \pm 0.15	0.17 \pm 0.08	0.16 \pm 0.21	0.35 \pm 0.15	0.17 \pm 0.19	0.69 \pm 0.33
ASSD \downarrow	2.96 \pm 2.29	4.35 \pm 1.54	6.70 \pm 2.85	4.16 \pm 1.28	5.24 \pm 1.42	3.01 \pm 2.13	1.89 \pm 0.69	0.97 \pm 1.19
Global Dice \uparrow	0.56 \pm 0.19	0.21 \pm 0.16	0.33 \pm 0.18	0.27 \pm 0.13	0.31 \pm 0.22	0.52 \pm 0.16	0.19 \pm 0.23	0.75 \pm 0.27
<i>Mixed lesions</i>								
Detection F1 (RQ) \uparrow	0.48 \pm 0.06	0.74 \pm 0.21	0.58 \pm 0.33	0.68 \pm 0.31	0.74 \pm 0.21	0.66 \pm 0.28	0.53 \pm 0.08	0.64 \pm 0.19
Instance Dice (SQ) \uparrow	0.33 \pm 0.13	0.46 \pm 0.17	0.35 \pm 0.23	0.36 \pm 0.21	0.46 \pm 0.21	0.37 \pm 0.18	0.42 \pm 0.14	0.62 \pm 0.18
Panoptic Dice (PQ _D) \uparrow	0.20 \pm 0.06	0.35 \pm 0.18	0.25 \pm 0.19	0.27 \pm 0.17	0.35 \pm 0.21	0.25 \pm 0.22	0.24 \pm 0.10	0.56 \pm 0.15
ASSD \downarrow	3.63 \pm 1.69	5.11 \pm 1.57	4.68 \pm 1.74	4.67 \pm 1.71	4.75 \pm 1.93	3.72 \pm 1.35	2.88 \pm 1.14	1.02 \pm 0.53
Global Dice \uparrow	0.25 \pm 0.14	0.48 \pm 0.16	0.33 \pm 0.23	0.35 \pm 0.20	0.46 \pm 0.19	0.32 \pm 0.21	0.29 \pm 0.01	0.62 \pm 0.20

Qualitative comparison.

Four representative cases are shown in Fig. 2: two where the method performs well and two that expose its limitations and typical failure modes of baselines⁵. Otsu produces large intensity-driven masks, useful with strong contrast (2) but prone to oversegment bright or noisy tissue (1, 3, 4). CAM-based methods yield coarse, discriminative activations, often capturing only part of a lesion (2, 4), with GradCAM++ highlighting small fragments (2) or responses across the vertebra (4). LayerCAM permits multiple components, but secondary responses reflect classifier bias toward benign findings, such as vertebra endplate or curvature. MedSAM frequently segments dark marrow or the entire vertebral body. AD produces fragmented residuals due to reconstruction errors and misses lytic lesions resembling fatty marrow conversion (2). The proposed method provides anatomically aligned masks across all rows, capturing diffuse blastic spread (1) and the major extent of a large lytic lesion (2). Remaining limitations include small holes in blastic regions (3, 4) and missed lytic components due to size filtering (4).

Phenotype-specific performance.

We stratify inferred masks by lesion type (appendix A.3.3). Lesion-wise precision–recall curves versus the Δ -score show a clear disparity: blastic lesions follow a clean precision–recall profile, whereas lytic lesions exhibit markedly noisier behavior. Lesion sizes follow the same pattern: blastic true positives are typically large (mean 225.9 pixels), while lytic true positives are substantially smaller (mean 52.4), and most lytic false positives are very small (mean 14.3).

Ablation studies.

We verified that the DAE reconstruction and healthy-edit process preserves vertebral anatomy (appendix A.4.1): reconstruction similarity was high (LPIPS 0.07, SSIM 0.97), and healthy edits remained structurally consistent with the originals (LPIPS 0.12, SSIM 0.83). To assess the contribution of the Δ -score, we compared it with the classifier’s raw malignancy probability (appendix A.4.2): the Δ -score achieved higher ROC–AUC for both blastic (0.93 vs. 0.90) and lytic lesions (0.62 vs. 0.50). Finally, appendix A.4.3 illustrates that projecting occluded images through the DAE removes masking artifacts, ensuring that downstream classifier responses are driven by anatomical content rather than by occlusion patterns.

⁵Additional examples and metrics appear in appendix A.3.2.

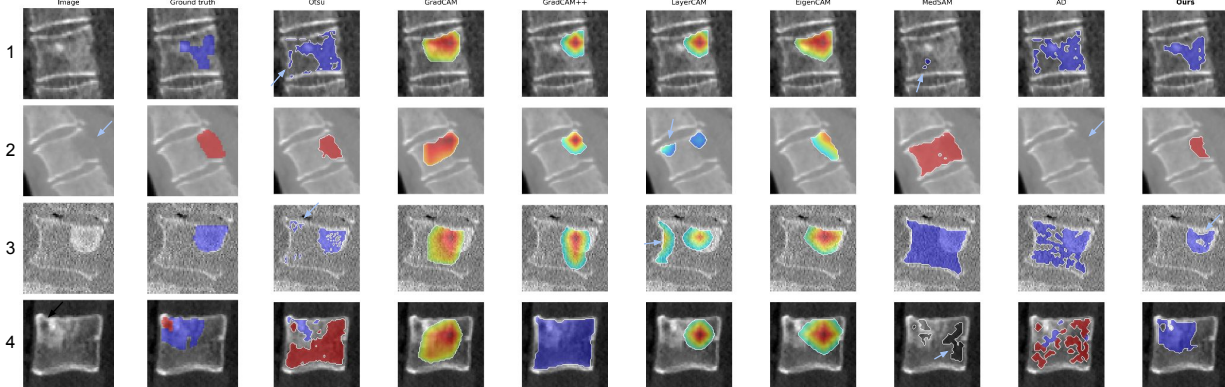


Figure 2: Qualitative comparison on four vertebral CT slices (rows). Columns show the input image, ground truth, evaluated baselines and our method. Blastic lesions are shown in blue, lytic in red. CAM-based results are thresholded heatmaps. The examples: (1) a diffuse blastic lesion with a bright focus, (2) a large lytic lesion with cortical breakthrough, (3) a blastic lesion in a grainy scan with imaging artifacts, and (4) a mixed case with a small lytic focus. Arrows indicate features referenced in the text.

6 Discussion

This work addresses vertebral metastasis segmentation using only vertebra-level labels, a setting in which existing weakly supervised methods often miss lesion extent or confuse malignant and benign patterns. The proposed combination of DAE-based healthy reconstruction and Hide-and-Seek attribution evaluates each candidate region independently, enabling lesion-level segmentation of lytic and blastic components without voxel-level supervision. The method identifies multiple lesions per vertebra and outperforms representative weakly supervised baselines across major metrics.

Comparison to baselines. The results highlight characteristic failure modes of intensity, CAM, foundation-model, and anomaly-detection baselines (Table 5 and Fig. 2). **Intensity-based thresholding** (Otsu) depends solely on voxel contrast and consequently oversegments bright or noisy tissue. **CAM-based approaches** are constrained by classifier discriminative capacity, highlighting only the most class-informative pixels rather than the full lesion extent. This matches their low Instance Dice and high ASSD variance, reflecting unstable and partial localization. LayerCAM can produce multiple disconnected masks, but secondary activations frequently reflect classifier biases toward benign structures. **MedSAM**, lacking malignancy semantics, tends to segment dark marrow or bright bone nonspecifically. **AD** relies on deviations from a healthy manifold and is therefore sensitive to reconstruction noise and prone to suppressing lytic lesions that resemble benign marrow patterns. Because a healthy-only generative model cannot reintroduce lesion features, AD cannot provide region-wise contribution testing.

Phenotype-specific considerations. The weaker performance on lytic lesions is consistent with their clinical ambiguity. Inter-rater agreement is substantially lower for lytic disease, reflecting its heterogeneous appearance and similarity to benign processes [26]. The classifier also receives weaker global evidence: lytic vertebrae show markedly lower malignant probabilities compared with blastic ones (appendix A.3.3). Combined with the predominance of very small candidate components, these factors explain the noisier Δ -score behavior and the reduced separability observed for lytic lesions.

Failures and limitations. Several limitations remain. (1) The editing trajectory and malignancy scoring depend on a classifier-derived semantic direction. When malignant evidence is weak, as often observed in lytic disease, both edits and Δ -scores become less reliable, consistent with lower classification probabilities and reduced detection performance. Conditional diffusion settings that directly generate healthy and malignant variants under explicit conditioning may reduce this dependency [40]. (2) The method further relies on contrast-polarity separation (D^+/D^-) and latent edits. Editing can introduce artifacts, particularly in very bright blastic regions, occasionally producing holed masks; post-processing may mitigate this [17]. Mixed lesions remain difficult because lytic and sclerotic components are often interwoven, making D^+/D^- an imperfect decomposition. Addressing mixed disease likely requires phenotype-aware editing rather than intensity-based separation. (3) The method assumes a patient-level phenotype label (lytic, blastic, mixed) derived from the primary cancer. As these labels determine which polarity is retained, mis-specified phenotypes can suppress true lesions or amplify false positives. A vertebra-level phenotype classifier could eliminate this dependency.

Clinical relevance and impact. Reliable delineation of vertebral metastases supports assessment of lesion burden, structural stability (e.g., SINS parameters [14]), canal compromise, and longitudinal progression. These tasks are difficult when multiple lesions coexist within a vertebra and qualitative comparison is inconsistent and time-consuming. Producing lesion-level masks from weak supervision may help standardize such assessments and provide quantitative measurements in settings where RECIST diameter criteria do not apply [12]. The framework also yields lesion-wise interpretability: each suspect is evaluated by its independent contribution to the malignancy score, producing calibrated attributions rather than diffuse heatmaps and extending counterfactual-style reasoning from classification to segmentation [4].

7 Conclusion and outlook

We presented a weakly supervised method for segmenting lytic and blastic vertebral metastases using only vertebra-level labels, combining diffusion-based healthy editing with a Hide-and-Seek strategy to isolate lesion-specific contributions. The approach outperforms representative weakly supervised baselines and provides anatomically grounded, lesion-level attribution, demonstrating that generative editing can yield accurate segmentation without voxel-level supervision.

Several extensions could further strengthen the framework. Moving from a single sagittal slice to a 3d formulation and incorporating pedicles or posterior elements may improve coverage and reliability in multilevel disease. Conditioning the generative model on malignancy phenotype could reduce dependence on a separately trained classifier, and a vertebra-level phenotype classifier would address the coarse assumption that each patient presents with a single dominant lesion type, as clinical cases often show mixed patterns across vertebrae. Finally, external validation on multi-center CT data will be essential to assess robustness.

Acknowledgments

This work received funding from the Deutsche Forschungsgemeinschaft (DFG, German Research Foundation) – Grant number 283653538 and the European Research Council (ERC) under the European Union’s Horizon 2020 research and innovation program (101045128-iBack-epic—ERC2021-COG). J.S.K. is cofounder and shareholder of Bonescreen GmbH. The other co-authors are not employees, cofounders, or shareholders of Bonescreen GmbH.

References

- [1] Chirag Agarwal and Anh Nguyen. Explaining image classifiers by removing input features using generative models. In *Proceedings of the Asian Conference on Computer Vision (ACCV)*, November 2020.
- [2] Nedra Amara and Said Gattoufi. Applying multiple instance learning for breast cancer lesion detection in mammography images. In *Proceedings of the 10th International Conference on Information and Communication Technologies for Ageing Well and e-Health - ICT4AWE*, pages 93–97. INSTICC, SciTePress, 2024.
- [3] Matan Atad, Vitalii Dmytrenko, Yitong Li, Xinyue Zhang, Matthias Keicher, Jan Kirschke, Bene Wiestler, Ashkan Khakzar, and Nassir Navab. Chexplaining in style: Counterfactual explanations for chest x-rays using stylegan. *arXiv arXiv:2207.07553*, 2022.
- [4] Matan Atad, David Schinz, Hendrik Moeller, Robert Graf, Benedikt Wiestler, Daniel Rueckert, Nassir Navab, Jan S. Kirschke, and Matthias Keicher. Counterfactual explanations for medical image classification and regression using diffusion autoencoder. *Machine Learning for Biomedical Imaging (Melba)*, 2(iMIMIC 2023 Special Issue):2024:024, 2024.
- [5] James Berenson, Lakshmi Rajdev, and Michael Broder. Pathophysiology of bone metastases. *Cancer Biology & Therapy*, 5(9):1078–1081, 2006.
- [6] C. Y. Chang, C. Buckless, K. J. Yeh, and M. Torriani. Automated detection and segmentation of sclerotic spinal lesions on body CTs using a deep convolutional neural network. *Skeletal Radiology*, 51(2):391–399, 2022.
- [7] Aditya Chattopadhyay, Anirban Sarkar, Prantik Howlader, and Vineeth N Balasubramanian. Grad-cam++: Generalized gradient-based visual explanations for deep convolutional networks. In *2018 IEEE Winter Conference on Applications of Computer Vision (WACV)*, pages 839–847, 2018.
- [8] Zhang Chen, Zhiqiang Tian, Jihua Zhu, Ce Li, and Shaoyi Du. C-cam: Causal cam for weakly supervised semantic segmentation on medical image. In *Proceedings of the IEEE/CVF Conference on Computer Vision and Pattern Recognition (CVPR)*, pages 11676–11685, June 2022.
- [9] Junlong Cheng, Jin Ye, Zhongying Deng, Jianpin Chen, Tianbin Li, Haoyu Wang, Yanzhou Su, Ziyang Huang, Jilong Chen, Lei Jiangand Hui Sun, Junjun He, Shaoting Zhang, Min Zhu, and Yu Qiao. Sam-med2d, 2023.
- [10] Jiri Chmelik, Roman Jakubicek, Petr Walek, Jiri Jan, Petr Ourednicek, Lukas Lambert, Elena Amadori, and Giampaolo Gavelli. Deep convolutional neural network-based segmentation and classification of difficult to define metastatic spinal lesions in 3d ct data. *Medical Image Analysis*, 49:76–88, 2018.
- [11] E. Edelmers, A. Nikuļins, K. L. Sprūdža, P. Stapulone, N. S. Pūce, E. Skrebele, E. E. Siņicina, V. Cīrule, A. Kazuša, and K. Boločko. AI-assisted detection and localization of spinal metastatic lesions. *Diagnostics*, 14(21):2458, 2024.

- [12] E.A. Eisenhauer, P. Therasse, J. Bogaerts, L.H. Schwartz, D. Sargent, R. Ford, J. Dancey, S. Arbuck, S. Gwyther, M. Mooney, L. Rubinstein, L. Shankar, L. Dodd, R. Kaplan, D. Lacombe, and J. Verweij. New response evaluation criteria in solid tumours: Revised recist guideline (version 1.1). *European Journal of Cancer*, 45(2):228–247, 2009.
- [13] Sarah C Foreman, David Schinz, Malek El Hussein, Sophia S Goller, Jürgen Weißinger, Anna-Sophia Dietrich, Martin Renz, Marie-Christin Metz, Georg C Feuerriegel, Benedikt Wiestler, et al. Deep learning to differentiate benign and malignant vertebral fractures at multidetector ct. *Radiology*, 310(3):e231429, 2024.
- [14] Daryl R. Fourney, Evan M. Frangou, Timothy C. Ryken, Christian P. Dipaola, Christopher I. Shaffrey, Sigurd H. Berven, Mark H. Bilsky, James S. Harrop, Michael G. Fehlings, Stefano Boriani, Dean Chou, Meic H. Schmidt, David W. Polly, Roberto Biagini, Shane Burch, Mark B. Dekutoski, Aruna Ganju, Peter C. Gerszten, Ziya L. Gokaslan, Michael W. Groff, Norbert J. Liebsch, Ehud Mendel, Scott H. Okuno, Shreyaskumar Patel, Laurence D. Rhines, Peter S. Rose, Daniel M. Sciubba, Narayan Sundaresan, Katsuro Tomita, Peter P. Varga, Luiz R. Vialle, Frank D. Vrionis, Yoshiya Yamada, and Charles G. Fisher. Spinal instability neoplastic score: An analysis of reliability and validity from the spine oncology study group. *Journal of Clinical Oncology*, 29(22):3072–3077, 2011.
- [15] Ziba Gandomkar, Pek Lan Khong, Amanda Punch, and Sarah Lewis. Using occlusion-based saliency maps to explain an artificial intelligence tool in lung cancer screening: Agreement between radiologists, labels, and visual prompts. *Journal of Digital Imaging*, 35(5):1164–1175, 2022.
- [16] Xueqi Guo, Yoshihisa Shinagawa, Sepehr Farhand, Halid Yerebakan, Kritika Iyer, Matthias Wolf, and Gerardo Hermosillo Valadez. Unsupervised abnormality segmentation in chest ct with anatomy-guided latent diffusion model and adaptive thresholding. In *Proceedings of the IEEE/CVF International Conference on Computer Vision (ICCV) Workshops*, pages 1017–1024, October 2025.
- [17] Limai Jiang, Ruitao Xie, Bokai Yang, Juan He, Huazhen Huang, Yi Pan, and Yunpeng Cai. Weakly supervised lesion localization and attribution for oct images with a guided counterfactual explainer model. *Expert Systems with Applications*, 287:128129, 2025.
- [18] Peng-Tao Jiang, Chang-Bin Zhang, Qibin Hou, Ming-Ming Cheng, and Yunchao Wei. Layercam: Exploring hierarchical class activation maps for localization. *IEEE Transactions on Image Processing*, 30:5875–5888, 2021.
- [19] Alexander Kirillov, Eric Mintun, Nikhila Ravi, Hanzi Mao, Chloe Rolland, Laura Gustafson, Tete Xiao, Spencer Whitehead, Alexander C. Berg, Wan-Yen Lo, Piotr Dollar, and Ross Girshick. Segment anything. In *Proceedings of the IEEE/CVF International Conference on Computer Vision (ICCV)*, pages 4015–4026, October 2023.
- [20] Florian Kofler, Hendrik Möller, Josef A. Buchner, Ezequiel de la Rosa, Ivan Ezhov, Marcel Rosier, Isra Mekki, Suprosanna Shit, Moritz Negwer, Rami Al-Maskari, Ali Ertürk, Shankeeth Vinayahalingam, Fabian Isensee, Sarthak Pati, Daniel Rueckert, Jan S. Kirschke, Stefan K. Ehrlich, Annika Reinke, Bjoern Menze, Benedikt Wiestler, and Marie Piraud. Panoptica – instance-wise evaluation of 3d semantic and instance segmentation maps, 2023.
- [21] Jun Ma, Yuting He, Feifei Li, Lin Han, Chenyu You, and Bo Wang. Segment anything in medical images. *Nature Communications*, 15(1):654, 2024.

- [22] Filipa Macedo, Katia Ladeira, Filipa Pinho, Nadine Saraiva, Nuno Bonito, Luisa Pinto, and Francisco Goncalves. Bone metastases: An overview. *Oncology Reviews*, 11(1):321, 2017.
- [23] Raghav Mehta, Fabio De Sousa Ribeiro, Tian Xia, Mélanie Roschewitz, Ainkaran Santhirasekaram, Dominic C Marshall, and Ben Glocker. Cf-seg: Counterfactuals meet segmentation. In *International Conference on Medical Image Computing and Computer-Assisted Intervention*, pages 117–127. Springer, 2025.
- [24] Masataka Motohashi, Yuki Funauichi, Takuya Adachi, Tomoyuki Fujioka, Naoya Otaka, Yuka Kamiko, Takashi Okada, Ukihide Tateishi, Atsushi Okawa, Toshitaka Yoshii, and Shingo Sato. A new deep learning algorithm for detecting spinal metastases on computed tomography images. *Spine (Phila Pa 1976)*, 49(6):390–397, 2024.
- [25] Mohammed Bany Muhammad and Mohammed Yeasin. Eigen-CAM: Visual explanations for deep convolutional neural networks. *SN Computer Science*, 2(1):47, January 2021.
- [26] Eunsun Oh, Hyun-joo Kim, Jong Won Kwon, Young Cheol Yoon, and Hyun Su Kim. Differentiation between spinal subchondral bone metastasis with focal pathologic endplate fracture and oedematous schmorl’s node. *Journal of Medical Imaging and Radiation Oncology*, 66(7):913–919, 2022.
- [27] Koji Onoue, Mai Yakami, Maho Nishio, Keita Nakane, Tetsuya Aramaki, Masashi Yakami, Kazuhiro Fujimoto, Yasushi Nagata, and Shogo Nishio. Temporal subtraction CT with non-rigid image registration improves detection of bone metastases by radiologists: results of a large-scale observer study. *Scientific Reports*, 11:18422, 2021.
- [28] Zhen Pan, Wenhui Huang, and Yuanjie Zheng. Mamba-based weakly supervised medical image segmentation with cross-modal textual information. In *proceedings of Medical Image Computing and Computer Assisted Intervention – MICCAI 2025*, volume LNCS 15967. Springer Nature Switzerland, September 2025.
- [29] Konpat Preechakul, Nattanat Chatthee, Suttisak Wizadwongsa, and Supasorn Suwajanakorn. Diffusion autoencoders: Toward a meaningful and decodable representation. In *IEEE Conference on Computer Vision and Pattern Recognition (CVPR)*, 2022.
- [30] Malika Sanhinova, Nazim Haouchine, Steve D. Pieper, William M. Wells III, Tracy A. Balboni, Alexander Spektor, Mai Anh Huynh, Jeffrey P. Guenette, Bryan Czajkowski, Sarah Caplan, Patrick Doyle, Heejoo Kang, David B. Hackney, and Ron N. Alkalay. Registration of longitudinal spine CTs for monitoring lesion growth. In Olivier Colliot and Jhimli Mitra, editors, *Medical Imaging 2024: Image Processing*, volume 12926, page 129262O. International Society for Optics and Photonics, SPIE, 2024.
- [31] Ramprasaath R. Selvaraju, Michael Cogswell, Abhishek Das, Ramakrishna Vedantam, Devi Parikh, and Dhruv Batra. Grad-cam: Visual explanations from deep networks via gradient-based localization. In *Proceedings of the IEEE International Conference on Computer Vision (ICCV)*, Oct 2017.
- [32] Lubdha M. Shah and Karen L. Salzman. Imaging of spinal metastatic disease. *International Journal of Surgical Oncology*, 2011(1):769753, 2011.
- [33] Tao Sheng, Tejas Sudharshan Mathai, Alexander Shieh, and Ronald M Summers. Weakly-supervised detection of bone lesions in ct. *Proceedings of SPIE–The International Society for Optical Engineering*, 12927:129270Q, 2024.

- [34] Danila Shvetsov, Johannes Ariva, Maxim Domnich, Raul Vicente, and Daniil Fishman. COIN: Counterfactual inpainting for weakly supervised semantic segmentation for medical images. In Luca Longo, Sebastian Lapuschkin, and Christin Seifert, editors, *Explainable Artificial Intelligence*, volume 2155 of *Communications in Computer and Information Science*. Springer, Cham, 2024.
- [35] Hristina Uzunova, Jan Ehrhardt, Timo Kepp, and Heinz Handels. Interpretable explanations of black box classifiers applied on medical images by meaningful perturbations using variational autoencoders. In Elsa D. Angelini and Bennett A. Landman, editors, *Medical Imaging 2019: Image Processing*, volume 10949, page 1094911. International Society for Optics and Photonics, SPIE, 2019.
- [36] Ostap Viniavskiy, Mariia Dobko, and Oles Doboševych. Weakly-supervised segmentation for disease localization in chest x-ray images. In Martin Michalowski and Robert Moskovitch, editors, *Artificial Intelligence in Medicine*, pages 249–259. Springer International Publishing, 2020.
- [37] Marc-André Weber, Alberto Bazzocchi, and Iris-M Nöbauer-Huhmann. Tumors of the spine: When can biopsy be avoided? *Seminars in Musculoskeletal Radiology*, 26(4):453–468, 2022.
- [38] Julia Wolleb, Florentin Bieder, Robin Sandkühler, and Philippe C. Cattin. Diffusion models for medical anomaly detection. In *Medical Image Computing and Computer Assisted Intervention – MICCAI 2022: 25th International Conference, Singapore, September 18–22, 2022, Proceedings, Part VIII*, page 35–45. Springer-Verlag, 2022.
- [39] Sung-Hoon Yoon, Hoyong Kwon, Jaeseok Jeong, Daehee Park, and Kuk-Jin Yoon. Diffusion-guided weakly supervised semantic segmentation. In *Computer Vision – ECCV 2024: 18th European Conference, Milan, Italy, September 29–October 4, 2024, Proceedings, Part XLVIII*, page 393–411. Springer-Verlag, 2024.
- [40] Lvmin Zhang, Anyi Rao, and Maneesh Agrawala. Adding conditional control to text-to-image diffusion models. In *Proceedings of the IEEE/CVF International Conference on Computer Vision (ICCV)*, pages 3836–3847, October 2023.

A Appendix

A.1 Implementation details

A.1.1 Hide-and-Seek attribution algorithm

Alg. 1 illustrates the procedure for identifying lytic lesions. Blastic lesions are derived in the same manner, except that the negative polarity of the difference map is used.

Algorithm 1: Hide-and-Seek attribution (lytic lesions example)

Input: Image I , semantic latent \vec{z} , classifier $c(\cdot)$, threshold τ
Output: Lytic segmentation mask M_{lytic}

```
 $\vec{z}_{\text{healthy}} \leftarrow \text{Eq. (1)}; \quad I_{\text{healthy}} \leftarrow \text{DAE}(\vec{z}_{\text{healthy}}); \quad // \text{ Healthy edit}$   
 $D \leftarrow I - I_{\text{healthy}}; \quad D^+ \leftarrow \max(D, 0); \quad // \text{ Difference map}$   
 $\{M^k\} \leftarrow \text{ConnectedComponents}(\text{Threshold}(D^+)); \quad // \text{ Lytic candidates}$   
Initialize  $C_{\text{lytic}} \leftarrow \emptyset$ ;  
for each mask  $M^k$  do  
     $I_{\text{hide}} \leftarrow \text{Eq. (2)};$   
     $\vec{z}_{\text{hide}}(M^k) \leftarrow \text{DAE}_{\text{enc}}(I_{\text{hide}}); \quad // \text{ DAE reconstruction + encoding}$   
     $\Delta(M^k) \leftarrow \text{as in Eq. (3)};$   
    if  $\Delta(M^k) \geq \tau$  then  
        Append  $M^k$  to  $C_{\text{lytic}}$ ;  
  
 $M_{\text{lytic}} \leftarrow \bigvee_{M^k \in C_{\text{lytic}}} M^k; \quad // \text{ Final lytic mask}$   
return  $M_{\text{lytic}};$ 
```

A.1.2 DAE training and hyperparameters

Table 3 provides hyperparameters used per step in the pipeline.

Table 3: Preprocessing, augmentation, DAE training and postprocessing hyperparameters

Parameter	Value
Preprocessing and augmentations	
Target voxel spacing	$0.8 \times 0.8 \times 0.8$ mm
Crop size	$64 \times 64 \times 64$ voxels
Orientation	PSR
Crop	Vertebra body mask + 5 voxel margin
Slice	Center crop to 5 sagittal slices, then random 1 slice
Augmentation probability	0.5
Rotation range	$\pm 33^\circ$ in-plane
Flip	Horizontal flip
Zoom range	0.85–1.15 in-plane
Gaussian noise	$\mu = 0.0, \sigma = 0.015$
DAE training and inference	
Batch size	8
Base channels	128
UNet channel multipliers	(1, 2, 4, 8, 8)
Encoder channel multipliers	(1, 2, 4, 8, 8, 8)
Learning rate	1×10^{-4}
Best scheduler	linear
Optimizer	Adam
Semantic latnet size (d)	512
T_{Semantic}	250
$T_{\text{Stochastic}}$	100
Hide-and-seek	
p_{healthy} (Eq. (1))	10^{-4}
Binarization threshold	mean
τ cutoff	0.5
Lesion mask postprocessing	
Crop	Vertebrae body mask - 2 voxel erosion
Filter	Masks < 5 pixels

A.1.3 Baseline implementation

Otsu thresholding. Lesion masks are obtained by applying thresholding using single- or multi-level thresholds depending on whether lytic, blastic, or mixed patterns are clinically expected.

GradCAM baselines. A ResNet-18 classifier is trained on the classifier subset dataset (AUC 0.94, F1 0.87). GradCAM, GradCAM++, LayerCAM, and EigenCAM [7, 18, 25, 31] are generated with the PyTorch Grad-CAM library⁶ from the one-before-last convolutional layer, and heatmaps are binarized via Otsu thresholding.

MedSAM. Using the official *vit_b* checkpoint [21], we create a loose bounding-box prompt by dilating the vertebral mask, run MedSAM once per vertebra, and restrict predictions to the eroded corpus.

Anomaly detection. The DAE is trained only on healthy vertebrae in the full dataset. At test time, malignant slices are reconstructed as pseudo-healthy images, residual maps are computed, and thresholded differences are post-processed into pseudo-lesion masks.

⁶<https://github.com/jacobgil/pytorch-grad-cam>

A.2 Dataset details

The dataset comprises 5,644 vertebrae from 440 patients (mean age 67.5 ± 12.9 years; 211 female, 229 male). It spans vertebral levels T1 through L5 and is highly imbalanced, containing predominantly healthy vertebrae (4,972 healthy; 672 malignant). During preprocessing, SpineR provides for each vertebra both an anatomical level label (T1–L5) and a vertebral corpus mask used for downstream analysis. Fig. A.2 summarizes the distribution of healthy and malignant vertebrae across thoracic and lumbar levels. Malignancies are more frequent in the lumbar spine. Fig. A.2 shows the distribution of manual lesion sizes for lytic and blastic phenotypes. These reference annotations span a broad range of sizes, whereas the 5-pixel threshold indicated applies only to *predicted components* during evaluation.

Figure 3: Distribution of healthy and malignant vertebrae across thoracic and lumbar levels.

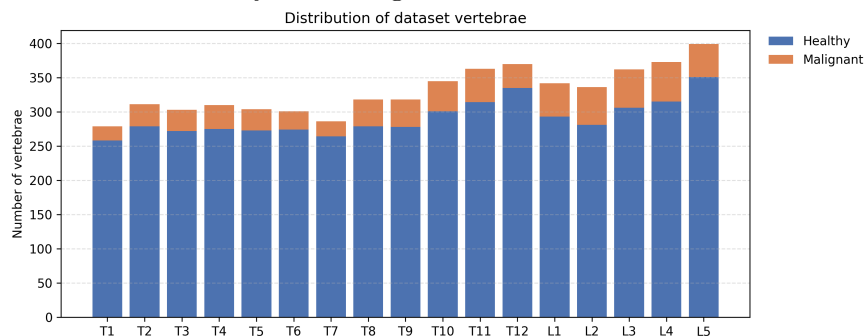
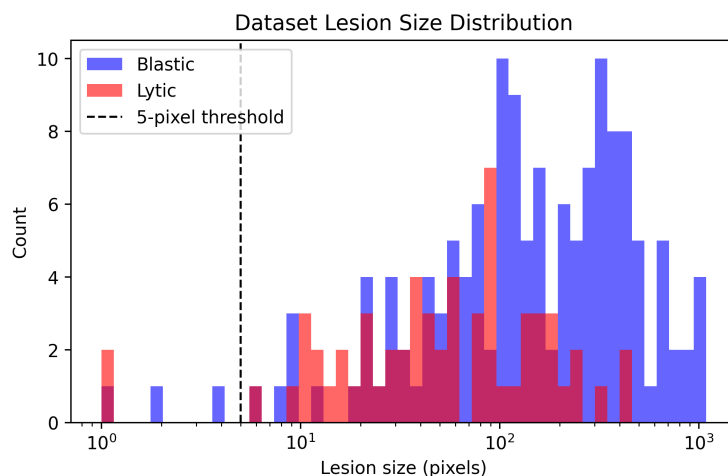


Figure 4: Log-scale histogram of manual lesion sizes (in pixels) for lytic (red) and blastic (blue) lesions. The dashed vertical line marks the 5-pixel threshold used as the minimum *predicted* lesion size in evaluation.



A.3 Additional results

A.3.1 Inter-rater agreement

Table A.3.1 summarizes detection and segmentation metrics for radiologist B relative to radiologist A. Agreement is high for blastic lesions, whereas lytic lesions show markedly lower consistency across all metrics. Table A.3.1 provides the underlying lesion counts, indicating that B recovers nearly all blastic findings from A, but misses a substantial portion of A’s lytic annotations (25% FN) and adds many additional lytic findings (45% FP), reflecting the inherent difficulty and subjectivity of identifying lytic metastasis.

Table 4: Quantitative inter-rater metrics (mean \pm SD) for radiologist B, evaluated against radiologist A as reference. Higher is better for all metrics except ASSD and RVD.

Metric	Blastic	Lytic
Detection Precision (\uparrow)	0.86 \pm 0.25	0.58 \pm 0.42
Detection Recall (\uparrow)	0.90 \pm 0.20	0.73 \pm 0.33
Detection F1 (RQ, \uparrow)	0.84 \pm 0.23	0.51 \pm 0.40
Instance Dice (SQ, \uparrow)	0.81 \pm 0.18	0.51 \pm 0.38
Panoptic Dice (PQ _D , \uparrow)	0.70 \pm 0.23	0.39 \pm 0.34
Global Dice (\uparrow)	0.82 \pm 0.16	0.49 \pm 0.37
ASSD (\downarrow)	1.19 \pm 0.91	1.00 \pm 0.49
RVD (SQ, \approx 0)	0.22 \pm 0.40	0.07 \pm 0.33

Table 5: Lesion-level agreement counts between radiologists A (reference) and B. “Matched” indicates lesions independently annotated by both raters. FN and FP rates reflect B’s misses and additional findings, respectively.

Metric	Blastic	Lytic
Annotated lesions (A)	142	61
Annotated lesions (B)	156	83
Matched (A) lesions	138	46
Missed (A) lesions (FN)	4	15
FN rate (%)	2.82%	24.59%
Extra (B) lesions (FP)	18	37
FP rate (per B)	11.54%	44.58%

A.3.2 Additional metrics and qualitative comparisons

Table A.3.2 reports complementary detection and volume-based metrics for all baselines and our method. Figure 5 provides additional qualitative examples.

Table 6: Detection precision, detection recall, and relative volume difference (RVD; close to zero is better) for all baselines and our method (mean \pm SD). Best scores per metric are in bold.

Metric	Otsu	GradCAM	GradCAM++	LayerCAM	EigenCAM	MedSAM	AD	Ours
<i>Blastic lesions</i>								
Detection Precision \uparrow	0.59 \pm 0.29	0.94 \pm 0.16	0.95 \pm 0.21	0.84 \pm 0.26	0.87 \pm 0.33	0.73 \pm 0.34	0.74 \pm 0.30	0.92 \pm 0.19
Detection Recall \uparrow	0.94 \pm 0.14	0.76 \pm 0.30	0.72 \pm 0.34	0.78 \pm 0.31	0.62 \pm 0.38	0.72 \pm 0.32	0.85 \pm 0.27	0.93 \pm 0.17
RVD ≈ 0	-0.18 \pm 0.21	0.37 \pm 0.96	0.80 \pm 1.89	0.19 \pm 2.48	0.59 \pm 1.50	0.84 \pm 1.80	0.12 \pm 0.84	0.05 \pm 0.41
<i>Lytic lesions</i>								
Detection Precision \uparrow	0.67 \pm 0.28	0.75 \pm 0.36	0.91 \pm 0.26	0.72 \pm 0.30	0.81 \pm 0.39	0.71 \pm 0.26	0.60 \pm 0.39	0.85 \pm 0.25
Detection Recall \uparrow	0.73 \pm 0.29	0.54 \pm 0.38	0.44 \pm 0.35	0.52 \pm 0.34	0.34 \pm 0.34	0.75 \pm 0.30	0.37 \pm 0.43	0.89 \pm 0.19
RVD ≈ 0	1.63 \pm 2.28	2.27 \pm 4.42	4.68 \pm 4.51	0.89 \pm 1.01	2.68 \pm 1.85	1.34 \pm 2.49	-0.43 \pm 0.20	-0.22 \pm 0.28
<i>Mixed lesions</i>								
Detection Precision \uparrow	0.41 \pm 0.05	1.00 \pm 0.00	0.82 \pm 0.38	0.89 \pm 0.31	1.00 \pm 0.00	0.69 \pm 0.33	0.56 \pm 0.06	0.68 \pm 0.14
Detection Recall \uparrow	0.81 \pm 0.06	0.63 \pm 0.28	0.49 \pm 0.34	0.59 \pm 0.34	0.63 \pm 0.28	0.72 \pm 0.30	0.78 \pm 0.22	0.75 \pm 0.12
RVD ≈ 0	3.33 \pm 3.85	1.90 \pm 3.03	1.11 \pm 2.13	0.91 \pm 1.92	2.03 \pm 3.14	0.59 \pm 1.54	0.33 \pm 0.21	0.51 \pm 0.66

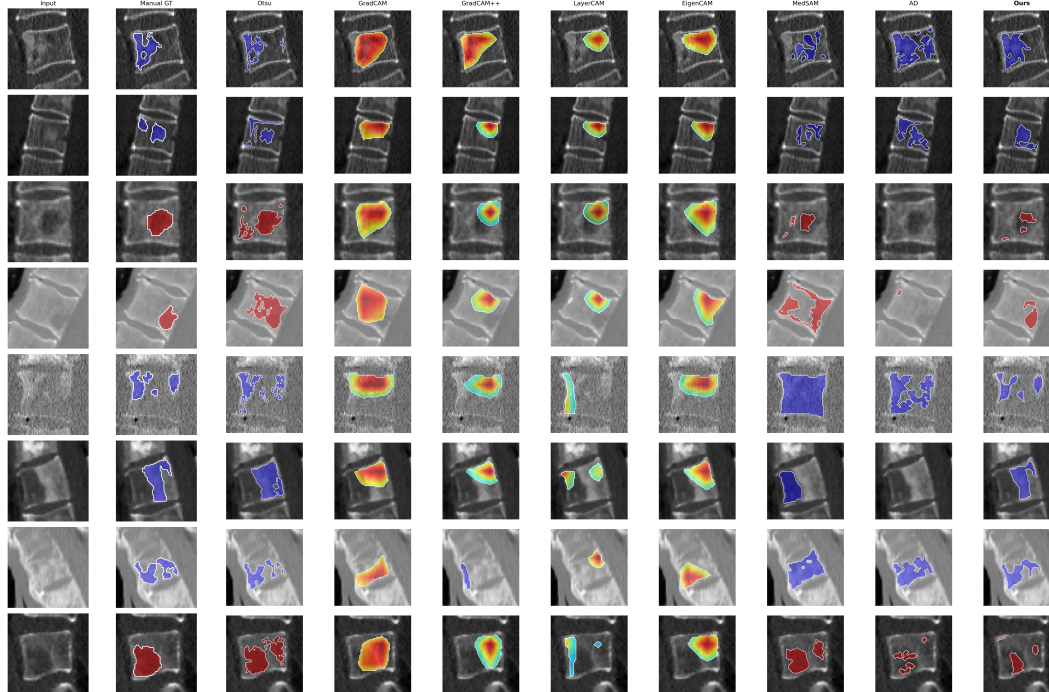


Figure 5: Qualitative comparison on eight vertebral CT slices (rows). Columns show the input image, manual ground truth, Otsu, CAM-based baselines, MedSAM, anomaly detection (AD), and our method.

A.3.3 Lesion-wise Delta-score Analysis

Figure 6 (left) shows precision–recall curves of the Δ -score stratified by phenotype. Blastic lesions exhibit strong separability, whereas lytic lesions produce a much noisier curve, consistent with the phenotype-specific results in the main text.

The scatter plots in Figure 6 (middle/right) relate lesion size to Δ on a per-lesion basis. Blastic true positives form a clear cluster of large lesions with high Δ , while blastic false positives are mostly small with lower scores. Lytic lesions show greater overlap, but true positives still tend to achieve higher Δ than false positives.

Table A.3.3 further summarizes lesion sizes and the original vertebra-level malignancy probability computed before any edits. Blastic vertebrae show substantially higher malignant probabilities than lytic vertebrae, indicating stronger global evidence available to the classifier. Lytic false positives are also extremely small on average, mirroring the scatter plots and the noisier precision–recall behavior. Together, these findings illustrate that Δ provides a meaningful lesion-level signal for both phenotypes, with stronger separation in blastic disease.

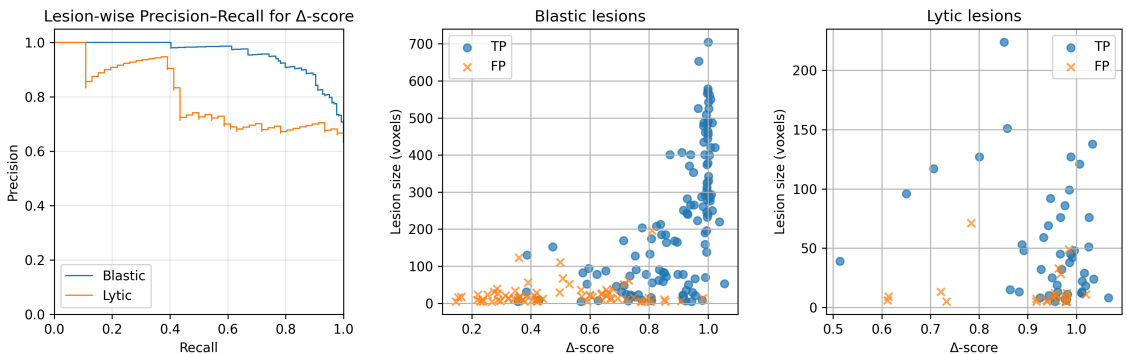


Figure 6: Left: precision–recall curves of the Δ -score for blastic and lytic lesions. Middle/right: lesion size versus Δ for blastic and lytic lesions (TPs blue points, FPs orange x’s). Blastic lesions show clearer separation between true and false positives, while lytic lesions exhibit greater overlap.

Table 7: Lesion sizes (mean \pm SD) and original vertebra-level malignancy probabilities, computed before any Hide-and-Seek editing. Blastic vertebrae show higher malignant probabilities, indicating stronger global classifier evidence compared to lytic vertebrae.

Metric	Blastic TP	Blastic FP	Lytic TP	Lytic FP
p_{orig}	0.932 ± 0.112	0.853 ± 0.158	0.777 ± 0.214	0.728 ± 0.252
Size (pixels)	225.9 ± 181.8	23.7 ± 29.6	52.4 ± 48.2	14.3 ± 16.0

A.4 Ablation studies

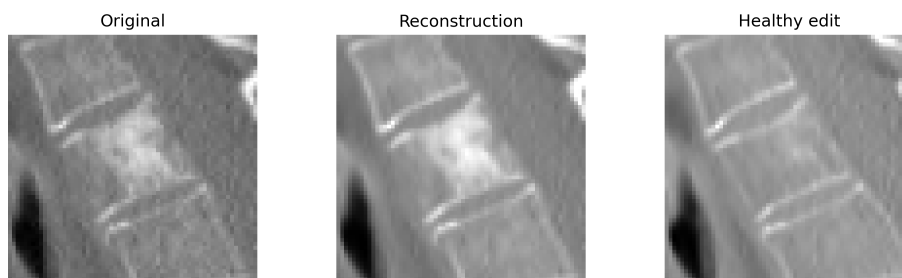
A.4.1 Reconstruction and Edit Quality

To assess whether the DAE preserves vertebral anatomy and produces plausible healthy edits, we report reconstruction and edit similarity metrics in Table A.4.1 and provide qualitative examples in Fig. A.4.1. The DAE achieves high fidelity when reconstructing the original, and healthy edits remain structurally consistent with the input while removing malignancy.

Table 8: Reconstruction and healthy–edit similarity. Lower LPIPS and higher SSIM indicate greater structural fidelity.

Setting	LPIPS ↓	SSIM ↑
Reconstruction (orig ↔ recon)	0.0675 ± 0.0319	0.9731 ± 0.0123
Healthy edit (orig ↔ edit)	0.1197 ± 0.0432	0.8336 ± 0.0641

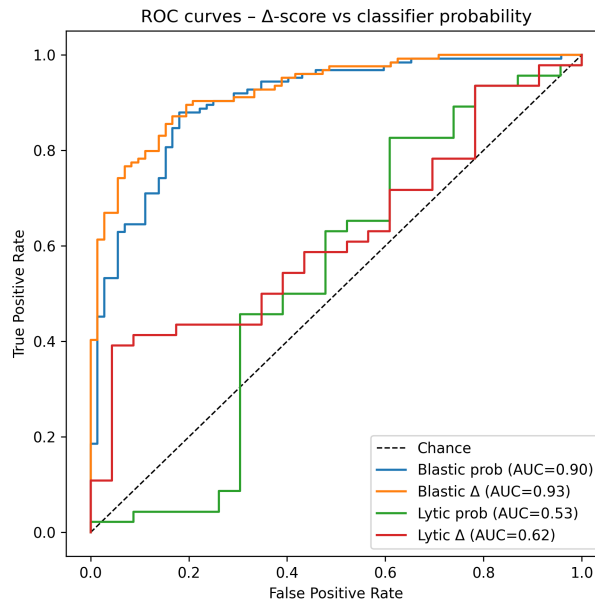
Figure 7: Qualitative examples of DAE behavior. From left to right: original slice, DAE reconstruction, and healthy edit produced by removing the malignant lesion.



A.4.2 Delta score vs. classifier probability

We compared the Δ -score with the classifier’s raw malignancy probability for distinguishing true from false positives. As shown in Fig. A.4.2, performance is similar for blastic lesions (ROC–AUC 0.93 vs. 0.90) but clearly improved for lytic lesions (0.62 vs. 0.50), with higher true-positive rates at comparable false-positive levels. This indicates that normalizing each lesion’s predicted probability by the malignancy of the original unedited image yields a more informative lesion-level signal than using the classifier probability alone.

Figure 8: ROC curves comparing the Δ -score and classifier probability for separating true and false positive regions. Results are shown for blastic and lytic lesions vs. chance.



A.4.3 Projection of occluded images

Fig. 9 shows examples of the original slice, the occluded image, and the corresponding projected image. Direct occlusion creates sharp masking artifacts that are visually unnatural. The projection step restores anatomically plausible appearance, producing edits that resemble real CT data.

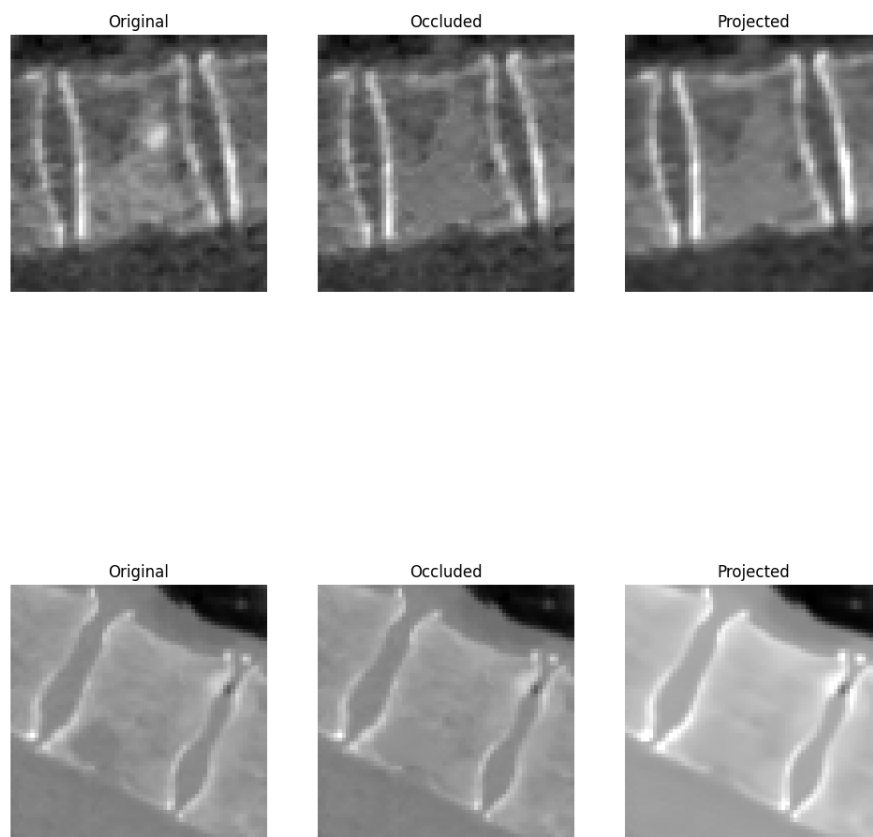


Figure 9: Examples illustrating the effect of projecting occluded images back onto the data manifold. Projection removes masking artifacts and restores plausible structure.